



The Synergistic Effect of Photoelectrochemical (PEC) Reactions Exemplified by Concurrent Perfluorooctanoic acid (PFOA) Degradation and Hydrogen Generation over Carbon and Nitrogen codoped TiO₂ Nanotube Arrays (C-N-TNTAs) photoelectrode

Yen-Ping Peng ^{a,*}, Hanlin Chen ^a, C.P. Huang ^{b,**}

^a Department of Environmental Science and Engineering, Tunghai University, Taichung 40704, Taiwan

^b Department of Civil and Environmental Engineering, University of Delaware, Newark, DE 19716, USA



ARTICLE INFO

Article history:

Received 4 January 2017

Received in revised form 23 February 2017

Accepted 28 February 2017

Available online 1 March 2017

Keywords:

Photoelectrochemical

C-N-TNTA

PFOA

Hydrogen

Synergetic effect

ABSTRACT

We studied the synergistic effect of photoelectrochemical reactions exemplified by concurrent oxidation of perfluorooctanoic acid (PFOA) and hydrogen generation over carbon and nitrogen codoped TiO₂ nanotube arrays (C-N-TNTAs) photoanode. The synthesized C-N-TNTAs were characterized by extended X-ray absorption fine structure (EXAFS) and X-ray diffraction (XRD) and results confirmed the successful doping of carbon and nitrogen into the TNTAs framework without altering its crystalline structure. Mott-Schottky analysis yielded a donor density of $3.547 \times 10^{18}/\text{cm}^3$ and $1.159 \times 10^{18}/\text{cm}^3$ for TNTA and C-N-TNTA, respectively. The photogenerated electrons had a lifetime (τ_{el}) of 2.52, 4.01, and 6.34 ms under biased potential of 0, 0.5, and 1.0 V (vs. Ag/AgCl), respectively, indicating the increase in lifetime of photogenerated electrons in photoelectrochemical (PEC) process. The synergistic effect was further quantified in terms of current/time profile at bias potential of 0 V at 1.1 mA and 1 V at 3.1 mA, individually. Results showed an increase in synergistic efficiency of 56 and 65% at a biased potential of 0.5 and 1.0 V, respectively. PEC effectively separated the photogenerated electron-hole pairs and enhanced the oxidation and reduction capability of the system. PFOA removal reached 56.1% in 180 min (initial concentration = 40 mg/L) over the C-N-TNTA photoanode in PEC mode. Results showed that perfluorooctanoate, $\text{C}_7\text{F}_{15}\text{COO}^-$, was first adsorbed on the C-N-TNTA anode surface followed by formation of $\text{C}_6\text{F}_{13}\text{COO}^-$ after losing CF_2 units. Results of electron spin resonance (ESR) further confirmed that reactive species such as $\cdot\text{OH}$ and $\text{CH}_3\cdot$ were responsible for the decomposition of PFOA during PEC reactions.

© 2017 Elsevier B.V. All rights reserved.

1. Introduction

It has been reported that highly ordered TiO₂ nanotube arrays (TNTAs) are effective for the degradation of refractory organic compounds in PEC systems [1,2]. The highly ordered structure enables considerable light absorption depth and enhances charge separation [3]. TiO₂ nanotube arrays have unique charge transport and carrier lifetime properties beneficial for a variety of applications, such as sensors [4], dye sensitized solar cells [5,6], hydrogen gen-

eration [7–9], CO₂ reduction [10], and supercapacitors [11]. When a bias potential is applied to an EC system, i.e., a PEC mode, indirect photocatalytic oxidation of contaminants is enhanced. There are reports on the enhancement of the degradation of hazardous chemicals by PEC systems [12–14]. However, little is done to quantify the synergistic effect of the PEC processes. The present study was to quantify the synergistic effect of photoelectrochemical reactions exemplified by the concurrent perfluorooctanoic acid (PFOA) degradation and hydrogen generation over a C-N-codoped TiO₂ nanotube arrays (C-N-TNTAs) photoanode.

Perfluorooctanoic acid (PFOA) is one of the most widely used perfluoroalkyl acids (PFAAs) for the synthesis of fluoropolymers and it has been reported that PFOA and related PFAAs, especially, perfluorooctanesulfonate (PFOS) are ubiquitous in the aquatic environment, wildlife, and humans [15,16]. PFOA and PFOS are suspected carcinogens and hormone disruptors [17,18]. Therefore,

* Corresponding author at: 40704 NO. 181, Section 3, Taichung Port Road, Taichung City, 40704, Taiwan.

** Corresponding author.

E-mail addresses: yppeng@thu.edu.tw (Y.-P. Peng), huang@udel.edu (C.P. Huang).

there PFOA was selected as a target chemical for study in the present research.

However, PFOA is resistant to biodegradation and conventional oxidation due to its strong carbon-fluorine bond ($C-F$, 116 kcal/mol)[19]. Hori et al. reported that direct photolysis of PFOA slowly produced CO_2 , F^- , and short-chain perfluorocarboxylic acids; H_2O_2 was less effective in PFOA decomposition [20]. Accordingly, numerous technologies such as membrane separation [21,22], adsorption [23,24], catalytic [20,25,26], and electrochemical (EC) [27–30] methods have been studied. Zhou et al. [27] studied the electrochemical degradation of PFOA over Ti/SnO₂-Sb-Bi anode and reported a 99% degradation at constant current of 0.25 A and initial PFOA concentration of 50 mg/L. Niu et al. [29] investigated the degradation of PFOA over a Ce-doped PbO₂ film anode and reported that perfluoroalkyl radicals reacted with hydroxyl radicals to form perfluoroalkyl alcohol, which then yielded perfluoroalkyl fluoride and ultimately resulted in a 95% mineralization of PFOA at an initial concentration of 100 mg/L.

The physical and chemical properties of C-N-TNTAs were characterized thoroughly by scanning electron microscopy (SEM), X-ray diffraction (XRD), X-ray photoelectron spectra (XPS), DRUV-vis, X-ray adsorption near-edge structure (XANES), and extended X-ray absorption fine structure (EXAFS). The lifetime of photogenerated electrons and the donor density were determined as to quantify the synergistic effect of PEC reactions exemplifying by the concurrent PFOA oxidation and hydrogen generation over the C-N-TNTA photanode. High-resolution LC-mass spectrometry was conducted to identify the degradation products as to establish the reaction pathways and kinetics.

2. Materials and methods

2.1. Synthesis of C-N-TNTA electrode

TiO₂ nanotube arrays were synthesized by anodization. High purity (95%) titanium foils (0.25 mm thick, Sigma-Aldrich) were anodized with a DC power supply (ITECH, IT6720, 0–5 A, 0–60 V) at a constant voltage of 30 V for 2 h in ethylene glycol electrolyte (99.8%, Sigma-Aldrich) containing 0.25 wt% of NH₄F (98.0%, Sigma-Aldrich) and 2 v% of H₂O. During anodization, titanium foil and platinum were the working and the counter electrode, respectively. After anodization, the titanium foil was sonicated in a mixed solution of acetone and ethanol (volume ratio 1:1), followed by rinsing with DI water and drying in a stream of air. All TNTA samples, initially amorphous, were annealed at 450 °C in air for 3 h to increase the crystallinity. The sintered samples were immersed in 20 mg/L of urea and then annealed at 450 °C again in an N₂ atmosphere to introduce carbon and nitrogen dopants.

2.2. Characterization of nanotube arrays

The crystal structure of C-N-TNTAs was characterized by XRD (Rigaku D/max-2500, Rigaku Corporation, Japan) with a Cu K α source of wavelength 0.154 nm. The JCPDS PDF card database was employed as a reference to identify XRD peaks. The microstructure and morphology of the synthesized materials were observed with scanning electron microscopy (Nova NanoSEM 430 FEI, USA). UV-vis spectrophotometry was performed to collect transmission and reflectance data using a Shimadzu 2550 UV-vis spectrometer (UV2401/2, Shimadzu, Japan). XPS experiments were performed with a PHI 5000 Versa Probe system (Physical Electronics, MN, USA). The binding energy of the XPS spectra was calibrated with the reference to the C1 s peak at 284.8 eV. All the ESR spectra were obtained using a Bruker ESR Spectrometer (Billerica, MA, USA) with 5,5-dimethyl-L-pyrroline-N-oxide (DMPO) as the spin

trapper at room temperature. Fifty μ L of control or sample solutions were put in glass capillary tubes with internal diameters of one mm and sealed. The capillary tubes were inserted into the ESR cavity, and the spectra were recorded at selected time. Other settings were as follows: 3485.00 G center field; 200.0 G sweep width; 9.777 GHz microwave frequency; 100 kHz modulation frequency; and 5.066 mW microwave power. To minimize measurement errors, the same quartz capillary tube was used throughout all ESR measurements. The XANES spectra of Ti K-edge were measured using BL-16A, at National Synchrotron Radiation Research Center (Hsinchu, Taiwan). The electron storage ring was operated at 1.5 GeV with a beam current of 300 mA. All reference materials and samples were deposited on one side of a piece of Kapton tape and placed in front of the X-ray beam to minimize self-absorption. The Ti K-edge absorption spectra were measured in a total X-ray fluorescence yield mode at room temperature. An Si (111) double crystal monochromator, of which the parallelism can be adjusted to eliminate the high order harmonics, was used to perform energy scans.

2.3. PEC experiments

All PEC experiments were carried out in three-electrode mode at room temperature, Ag/AgCl electrode as reference electrode, C-N-TNTA as working electrode (2.25 cm²) and Pt wire (0.5 mm dia., 99.99%, Fisher Scientific, pretreated by alternatively polarizing at 10 V in 0.1 M of H₂SO₄ solution) as counter electrode. A self-designed H-type reactor with separate anode and cathode chambers was used to study PFOA degradation. The anodic and cathodic chambers were connected with a cation-exchanged membrane (DuPont™ Nafion® 212) to maintain electroneutrality in the system. A quartz window (7 cm²), on the side of the anode chamber, provided good optical quality. Linear sweep voltammetry was performed with a voltage scan speed of 0.01 V/s. Electrochemical impedance spectroscopy (EIS) was performed under open circuit voltage over a frequency range from 10 kHz to 10 mHz with an AC voltage of 5 mV. The potential for I-V and I-t measurements and for PEC degradation experiments were controlled by an electricity workstation (AutoLAB PGSTAT302N, Holland).

2.4. Analytical methods

Concentration of PFOA and its decomposition products were analyzed by HPLC (Agilent 1200 Series, USA) using an Agilent ZORBAX Eclipse Plus C₁₈ reversed phase column (2.1 × 100 mm, 1.8 μ m). The column oven temperature was set to 40 °C. The flow rate was maintained at 0.2 mL/min with a mobile phase of eluent A (acetonitrile) and B (10 mmol/L ammonium acetate/water). The eluent gradient started with 40% A and 60% B for 9.0 min and then was linearly increased to 90% A and 10% B over 3.0 min. Chromatographically separated samples were analyzed in negative ion monitoring mode for PFOA (m/z = 369), PFHpA (m/z = 319), PFHxA (m/z = 269), PFPeA (m/z = 219), PFBA (m/z = 169), and PFPrA (m/z = 119) (Table S1, Supporting Information). Operational conditions were as follows: the sheath gas (N₂) pressure was 0.4 MPa (35psi). The capillary potential was –4.0 kV. The source temperature was 120 °C and the desolvation temperature was 350 °C. An electrospray negative ionization mode was used to identify the products in the liquid phase. The analysis was carried out in multiple-reaction monitoring mode.

The F[–] concentration was determined by ion-chromatograph system (Dionex ICS-1000, USA) consisting of an automatic sample injector (sample injection volume: 25 μ L), a degasser, a pump, a guard column (Dionex AG22, 4 × 50 mm, USA), a separation column (Dionex AS22, 4 × 250 mm, USA), a column oven (30 °C), and a conductivity detector with a suppressor device. The mobile phase

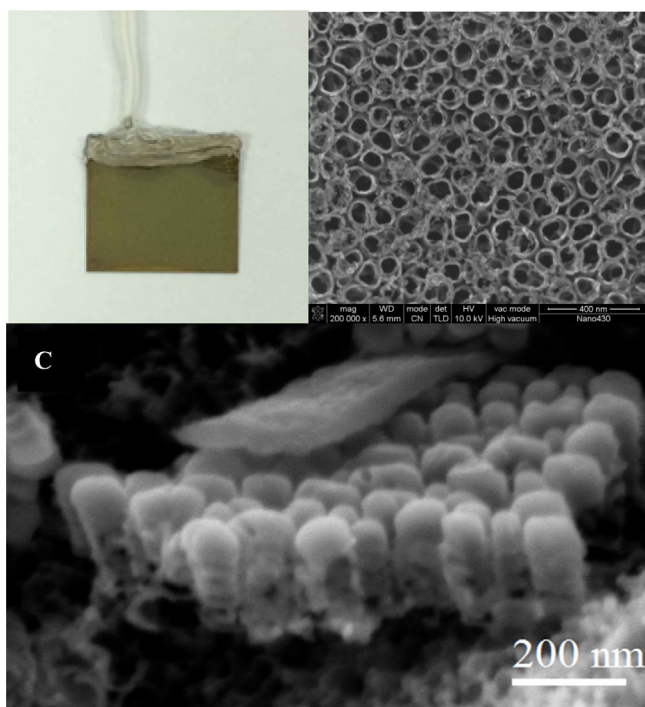


Fig. 1. (a) C-N-TNTA photoanode, (b) typical FESEM image of nanotube arrays (top view), and (c) typical FESEM image showing the cross-sectional view of C-N-TNTA.

was composed of Na_2CO_3 (4.5 mM) + NaHCO_3 (1.4 mM) and the flow rate was set at $1 \text{ mL} \cdot \text{min}^{-1}$.

3. Results and discussion

3.1. Characterization of C-N-TNTA electrodes

Fig. 1a shows the picture of the as-synthesized C-N-TNTA electrode. The SEM images in **Fig. 1b & c** show that the C-N-TNTA was well-aligned and organized into uniform arrays. After carbon and nitrogen codoping, the nanotubular structure of TiO_2 retained its integrity with no significant morphological changes. The top of the tube open was *ca.* 90–100 nm in diameter and *ca.* 200 nm in length. Highly ordered, vertically oriented TiO_2 nanotube arrays constitute a material architecture that offers a large internal surface area without concomitant decrease in geometric and structural order. The precisely oriented nature of such nanotube arrays makes them excellent electron percolation pathways for easy charge transfer between interfaces. Moreover, film feature with high PC reactivity and strong stability, such as C-N-TNTA film, can serve as photoanodes. It has been reported that TNTA photoanodes evidently enhance fuel cell performance compared to nano- TiO_2 film electrodes and that TNTA-based PEC system is a promising technology for wastewater treatment and fuel cell systems [1].

Fig. S1 illustrates the XRD pattern of typical C-N-TNTA samples. After being sintered at 450°C , the C-N-TNTA structure showed peaks at 25° , 38° , 54° , and 63° , corresponding to anatase TiO_2 as matched with JCPDS-784486 (PDF 21-1272). No rutile peak was observed. UV-vis absorption spectra were used to calculate the band gap (Fig. S2) according to the Tauc formula: $(\alpha h\nu)^{1/n} = \beta h\nu - E_g$ and $h\nu = 1240/\lambda$; where h is the discrete photon energy; λ is the wavelength; α is the absorption coefficient; and β is the absorption constant; n is dependent on the characteristics of the transition in a semiconductor; $n=2$ for indirect interband transition (e.g., TiO_2). The inset in Fig. S2 gives band gap of 3.2 and 2.9 eV for TNTA and C-N-TNTA, respectively. The short band gap of C-N-TNTA was attributed to the additional states conferred by

carbon and nitrogen doping [31–34]. As demonstrated in Fig. S2, the absorbance shoulders for C-N-TNTA samples exhibited a high absorbance wavelength at 425 nm, which indicated the visible light photosensitivity nature of C-N-TNTA and the formation of an intra-band gap located above the valence band that resulted from the interstitial introduction of carbon and nitride codoped into the oxide lattice and the substitution of oxide centers by nitride centers [35]. Four high-resolution XPS scans, namely, Ti 2p (Fig. S3a), N 1s (Fig. S3b), C 1s (Fig. S3c), and O 1s (Fig. S3d), revealed the states of the chemical bonding (and the surface concentrations of nitrogen) near the film surface. Fig. S3a shows that Ti 2p spectra had two peaks near 458.8 eV (Ti 2p3/2) and 464.2 eV (Ti 2p1/2). The Ti 2p region was of Ti^{4+} state, which was confirmed by the oxidation of Ti to TiO_2 . The N 1s spectrum at peak 400.1 eV was attributed to the N–Ti–O bond. Furthermore, one peak centered at approximately 399.6 eV, indicating the formation of oxynitrides such as Ti–N–O and Ti–O–N [36,37]. Dai et al. only observed one new peak at 400.1 eV in the N 1s spectrum of C and N codoped nanoscale TiO_2 nanosheets, indicating the presence of N–Ti–O linkages [38,39]. Notably, the doping linkage may be different, depending on the synthesis methods and nitrogen sources. The appearance of N 1s spectra showed that chemical deposition could successfully dope nitrogen into the TiO_2 structure. XPS analysis showed that the atomic nitrogen concentration was 0.82%. Results of XPS and UV-vis analyses indicated that the band gap reduction was created by the additional states brought by carbon and nitrogen doping. Fig. S3c shows two peaks positioned at approximately 284.8 and 286.5 eV. The peak at 284.8 eV is assigned to elemental carbon and the peak at 286.5 eV is attributed to C–O bands. Similarly, regarding the O1s XPS spectra, the peak at 529.8 eV is ascribed to the Ti–O bonds and the peak at 531.5 eV is the O atoms bonded to N or C in the form of carbonate species or oxynitrides [37]. In conclusion, carbon and nitrogen were successfully doped into TNTA.

XANES was employed to observe the local structure of C-N-TNTAs. **Fig. 2a** and **Fig. 2b** show the Ti K-edge XANES and FT-EXAFS spectra of C-N-TNTAs and P25 TiO_2 , respectively. As shown in **Fig. 2a**, for the Ti K-edge spectra of TiO_2 P25, the characteristic pre-edge peaks were in the range from 4960 to 4980 eV; in general, the peaks arose from hybridization of p and d orbitals of Ti atom and surrounding neighbors [40,41]. A peak at 4968 eV was attributed to the quadrupole transition of $1s \rightarrow t_{2g}$ states of octahedral TiO_6 , associated with Ti 3d – 4p hybridized states [42]. Peaks at 4972 and 4974 eV could be ascribed to the $1s \rightarrow 3d$ transition and designated as $1s \rightarrow t_{2g}$ and $1s \rightarrow 3e_g$ transitions, individually [43,44]. By contrast, Ti K-edge spectra of C-N-TNTA exhibited an intense pre-edge peak at 4967 eV, corresponding to dipolar-allowed transitions that happened as $1s \rightarrow t_{2g}$ molecular levels developed from 3d and 4p Ti orbitals and neighboring orbital [45]. Similar Ti K-edge XANES spectra were observed for Ti-oxide/Y-zeolite; the strong signal pre-edge peak suggests that Ti-oxides in C-N-TNTAs are tetrahedral [46]. Fourier transformation (FT) of EXAFS spectra from CN-TNTA and TiO_2 (P25) are shown in **Fig. 2c**. In FT-EXAFS spectra of TiO_2 (P25), the peaks a, b, and c represent Ti–O, Ti–Ti, and Ti–O–Ti coordination shells, respectively [47]. Two signals near 1.56 and 2.46 Å can be assigned to oxygen molecules that neighbor Ti–O monomers. The peak intensity of C-N-TNTA was lower than that of TiO_2 (P25), illustrating greater crystallinity of TiO_2 (P25) than C-N-TNTA. **Fig. 2c** compares the FT-EXAFS of C-N-TNTA and TNTA. The radial distance of peaks at 1.53, 2.46, and 4.95 Å are almost the same for both C-N-TNTA and TNTA, which may be attributed to the similarity of atomic size of O (1.52 Å), C (1.7 Å), and N (1.55 Å), leading to structure of similar length. The results of EXAFS confirmed the XRD finding that doping carbon and nitrogen into TNTA structures did not change the crystallinity levels.

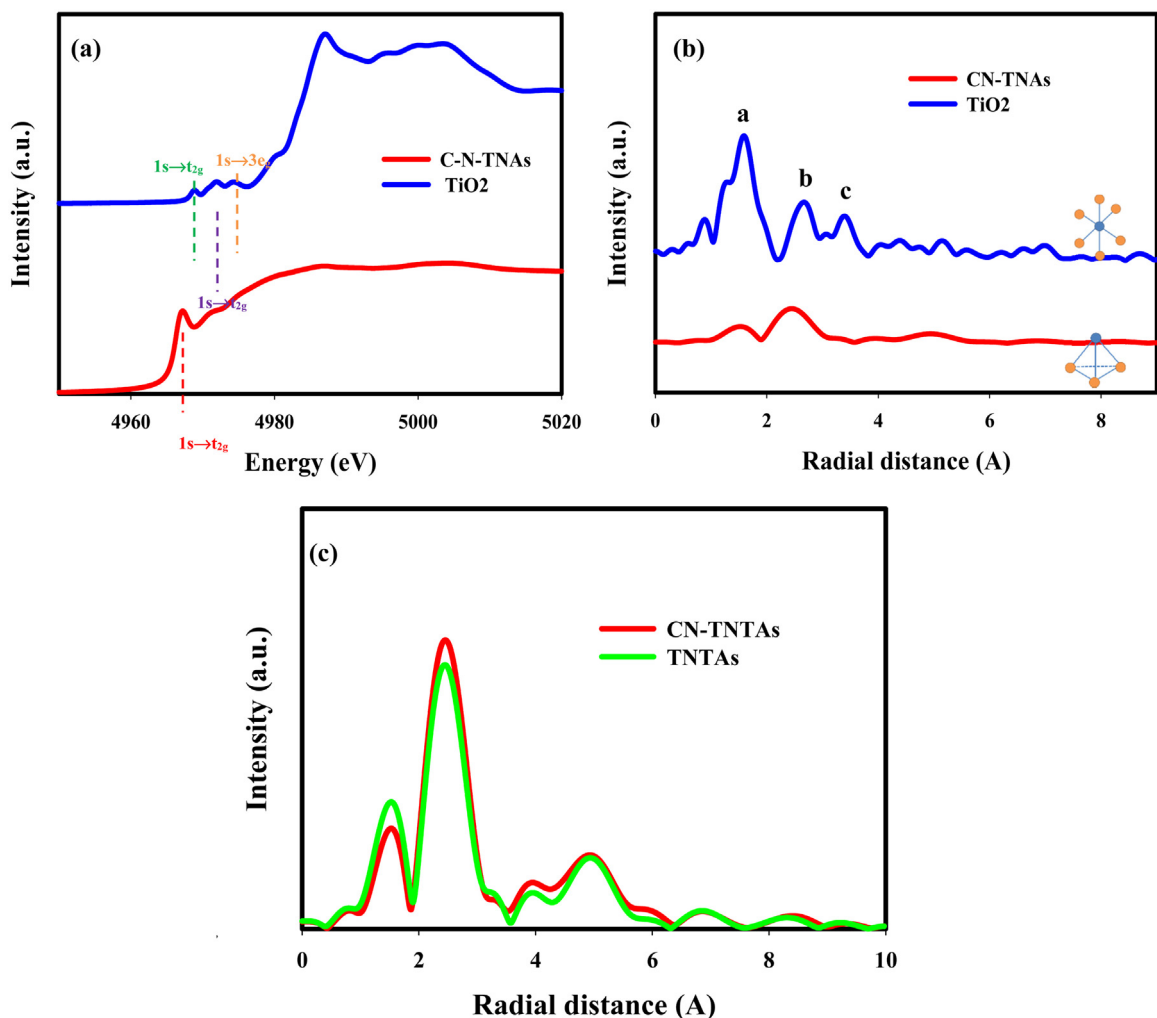


Fig. 2. (a)XANES, (b)FT-EXAFS spectra of C-N-TNA and P25 TiO₂ and (c) FT-EXAFS spectra of C-N-TNA and TNA.

3.2. PEC characteristics of the C-N-TNTA electrode

The transient photocurrent responses at three bias potentials, namely, 0, 0.5, and 1 V vs. Ag/AgCl, were recorded during several on-off illumination cycles. As shown in Fig. S4, the photocurrent decreased to nearly zero as soon as the light was turned off and reached 1.1, 2.5, and 3.1 mA/cm² when the light was on and applied voltage was at 0, 0.5, and 1 V (vs. Ag/AgCl), respectively. The applied bias potential did successfully separate and isolate the photogenerated electrons and holes.

Fig. 3 shows the typical Nyquist plot of C-N-TNTA under 3.12 mW/cm² of illumination at different applied voltages in 0.1 M NaCl solution [48–51]. The curvature of the EIS followed the order: 1.0 V > 0.5 V > 0.0 V. A large curvature is indicative of effective separation of photogenerated electron–hole pairs [50,51], which will enhance pollutant degradation efficiency.

Fig. 4 shows the Bode phase plot at frequency between 0.1 and 10³ Hz. The electron lifetime, τ_{el} , is inversely proportional to the peak frequency f_p according to the equation [52]: $\tau_{el} = 1/2\pi f_p$. Table S2 (Supporting Information) shows the peak frequency and estimated electron lifetime (τ_{el}) of C-N-TNTA were 63.1, 39.8 and 25.1 Hz and 2.52, 4.01, and 6.34 ms at 0, 0.5, and 1.0 V, respectively. The results revealed that the electron lifetime (τ_{el}) of photoexcited electrons at 1.0 V was approximately 2.52 and 1.58 times larger than that at 0 V and 0.5 V, respectively. Ye et al. [53] reported a τ_{el} of 10.05 ms for hierarchically structured TNTA, fabricated by electro-

chemical anodization and hydrothermal treatment. Results of Bode phase plot agreed well with that of Nyquist plot, indicating that bias potential could reduce the recombination of photogenerated electrons and holes thereby extending the electron lifetime.

The donor density can be calculated from the slope of Mott–Schottky plot according to the following equation:

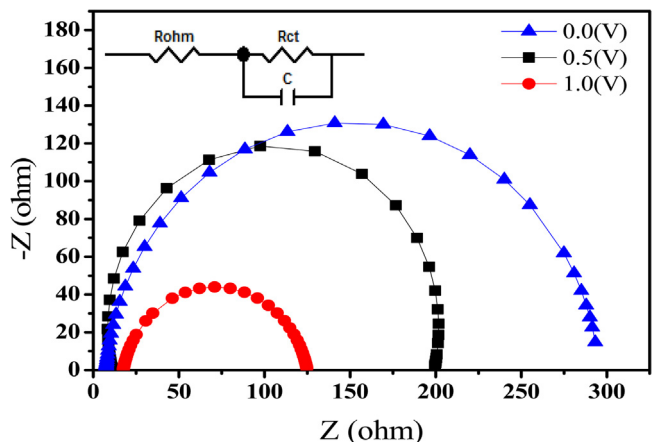


Fig. 3. Nyquist plot of C-N-TNTA at different applied voltage in 0.1 M NaCl solution with 100W low-pressure Hg illumination at room temperature.

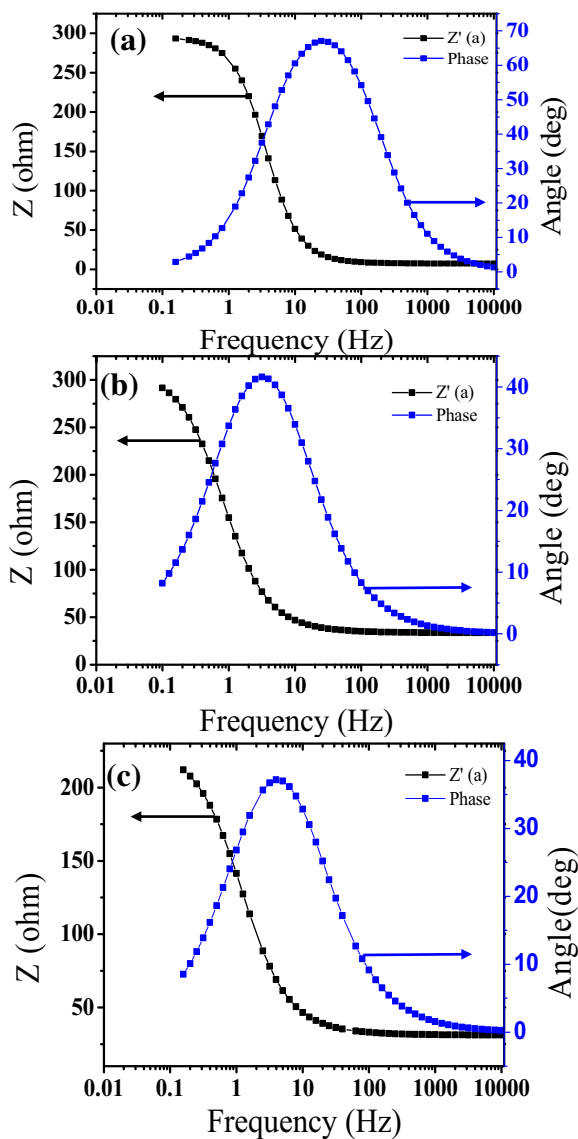


Fig. 4. Bode phase plot of C-N-TNTA at (a) 0 V, (b) 0.5 V and (c) 1 V.

$N_d = (2/e\epsilon\epsilon_0)[d(1/C^2)/dV]^{-1}$; where C is the differential capacitance of the Helmholtz layer; e is the electron charge; ϵ is the relative dielectric constant of TiO_2 ($\epsilon = 10$) [54–56]; ϵ_0 is the permittivity of vacuum; V is the applied bias at the electrode; and N_d is the donor density. Fig. 5 shows the Mott–Schottky plot of $1/C^2$ as a function of the applied potential, which gave positive slope suggesting C-N-TNTA an n -type semiconductor. The donor density was $1.159 \times 10^{18} \text{ cm}^{-3}$ and $3.547 \times 10^{18} \text{ cm}^{-3}$, for TNTA and C-N-TNTA, respectively. Results clearly indicated that carbon and nitrogen doping of TNTA increases donor density by a factor of three. The Mott–Schottky slope of C-N-TNTA was smaller than that of TNTA, suggesting the increase in capacitance upon C and N co-doping. The larger N_d of C-N-TNTA signified that it was a faster carrier for charge transfer than TNTA and thus enhanced PEC performance [49]. As illustrated in Fig. 5, the E_{fb} was -0.4 and -0.49 V (vs. Ag/AgCl) for TNTA and C-N-TNTA, respectively. The exceptionally low E_{fb} for C-N-TNTA indicates a very efficient charge separation and transportation [55]. The band bending and the formation of a space charge layer (Schottky barrier) is important to the semiconductor/electrolyte interface (SEI) [57]. The space

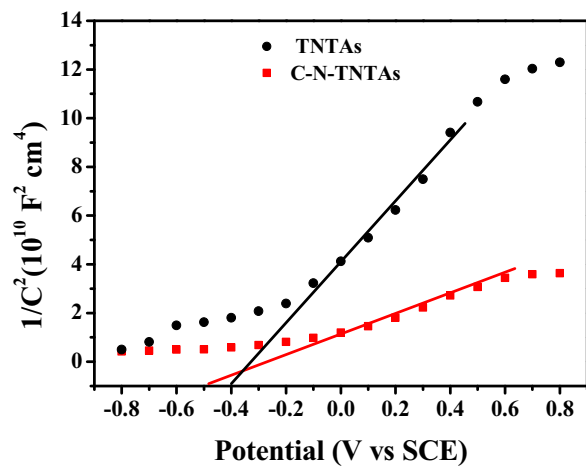


Fig. 5. Mott–Schottky plot of TNTA and C-N-TNTA collected at a frequency of 100 Hz.

charge layer is derived from the Mott–Schottky plot through the expression:

$$W = [2e\epsilon_0(E - E_{fb})/\epsilon_0 N_d]^{1/2}$$

Where W is the space charge thickness; E is the applied potential at the working semiconductor electrode. At an applied potential of 0, 0.5 and 1.0 V (vs. Ag/AgCl) the calculated space charge layers were found to be 390, 555 and 681 nm, respectively, indicating that applied bias potential in PEC system could increase the thickness of space charge layer leading to efficient electrochemical reactions. The results of both Nyquist plot and Bode plot indicated that the photogenerated electron–hole pairs could be effectively separated by increasing the applied bias potential. An increased charge transfer tends to increase the electron lifetime, which in turn will enhance the degradation of specific organic compounds.

Fig. 6 gives results of ESR analyses for TNTA (Fig. 6a) and C-N-TNTA (Fig. 6b), respectively. Fig. 6a shows a peak intensity of 1:2:2:1 upon illumination of TNTA indicating the continuous generation of DMPO–•OH. Fig. 6b shows the formation of methyl radicals upon light irradiation over C-N-TNTA. A characteristic DMPO–•CH₃ adduct had a peak intensity of 1:1:1:1:1 [58] indicating formation of DMPO-OH adduct upon UV illumination. The hole–electron pairs produced under UV irradiation and electric fields excited valence band electrons (e_{VB}) to the conduction band, yielding valence band holes (h_{VB}) and producing •OH radicals at the photoanode surface. The latter process is implicated in the PEC decomposition of pollutants [59]. Notably, the characteristic DMPO–•CH₃ adduct had a peak intensity of 1:1:1:1:1. No such signals were observed in the dark. These signals represented the presence of predominantly strong oxidation species responsible for PEC reactions. Our result was the same as reported by Pan et al. [60] who demonstrated the presence of •OH and CH₃ • radicals and above strong oxidants as the predominant species during PC reactions on the surface of Mn_{0.5}Zn_{0.5}Fe₂O₄/TiO₂ electrode [60]. It is generally known that the highly oxidizing (surface-bound) •OH radical, derived from the oxidation of chemisorbed OH[−] or H₂O by photogenerated h_{VB}, is the main oxidative species acting in the PC degradation of organic pollutants [61]. Some reactions can also be triggered by direct hole oxidation, especially when the chemical contaminants are at high concentrations and high adsorption density on the photocatalyst surface [62].

3.3. Quantify the synergistic efficiency of the PEC process

The total number of electrons (e^-_T) in the PEC system can be described as:

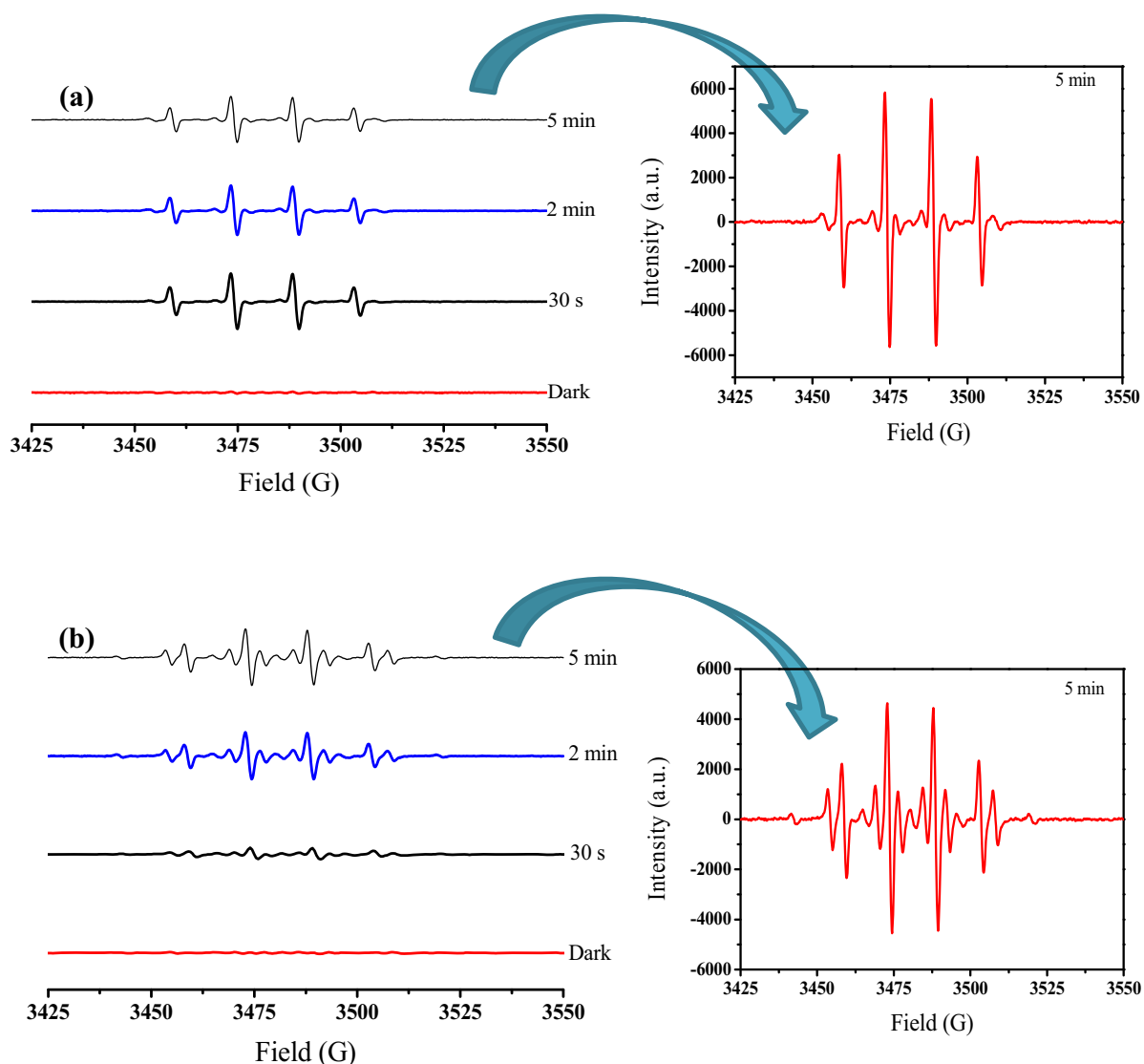


Fig. 6. (a) Degradation PFOA by different methods, (b) production of shorter-chain intermediates as a function of time produced during PFOA decomposition, (c) decomposition and defluorination of PFOA. (PFOA concentration was 40 mg/L, light source was 100W low-pressure Hg light and the applied voltage in PEC and EC process was 1.0 V vs. Ag/AgCl).

$e_T^- = e_{C-N-TNTA}^- + e_b^-$, where $e_{C-N-TNTA}^-$ is electrons generated photo-chemically and e_b^- is electrons generated by external bias potential ($e_b^- = V_b/R$, where V_b is bias potential; R is system resistance). The e_b^- value can be monitored at different bias potentials against dark current; accordingly, the e_T^- value was 0.0012, 0.023, and 0.033 mA at bias potentials of 0.0, 0.5, and 1.0 V, respectively. Consequently, the $e_{C-N-TNTA}^-$ value was 1.1, 2.5, and 3.1 mA at the bias potential of 0.0, 0.5, and 1.0 V, respectively (Table 1). The synergistic effect efficiency (σ) can be evaluated by the following equation: $\sigma(\%) = \left(\frac{I_v - I_0}{I_T} \right)$; where I_v is the photocurrent at given bias potential, (e.g., 0.5 and 1.0 V in this study); I_0 and I_T are the photocurrent at 0 V bias potential and the total current measured at given bias potential, respectively. The synergistic effect efficiency (%) was 0, 56, and 65% at 0, 0.5, and 1.0 V, respectively (Table 1). In general, same degree of irradiation will produce same amount of photocurrent. However, the photocurrent was increased with increase in bias potential, the driving force for photogenerated electrons, which suggested that the greater the applied bias potential, the larger the decrease in hole-electron recombination. Furthermore, an external potential (than the redox potential of the

Table 1
Pseudo-first-order rates constant of PFOA degradation (k_{obs}) under different processes at pH 4.

	Rate constant (k_{obs} , s^{-1})	R^2
Processes		
P	0.4×10^{-3}	0.9791
PC	1.1×10^{-3}	0.9907
EC	0.4×10^{-3}	0.9781
PEC	4.3×10^{-3}	0.9898
Different bias potentials (V)		
0.0	1.4×10^{-3}	0.9761
0.5	2.1×10^{-3}	0.9913
1.0	4.3×10^{-3}	0.9898

contaminant chemical species of interest) can provide a greater anodic current to promote the EC oxidation reaction. PEC can effectively degrade aqueous pollutants via the synergistic effect of EC (direct anodic) and PC (indirect) oxidation [12].

Our results clearly proved the concept of synergistic effect in a two-chamber PEC system and quantified the effect of photogenerated current and hole on PEC oxidation for the first time.

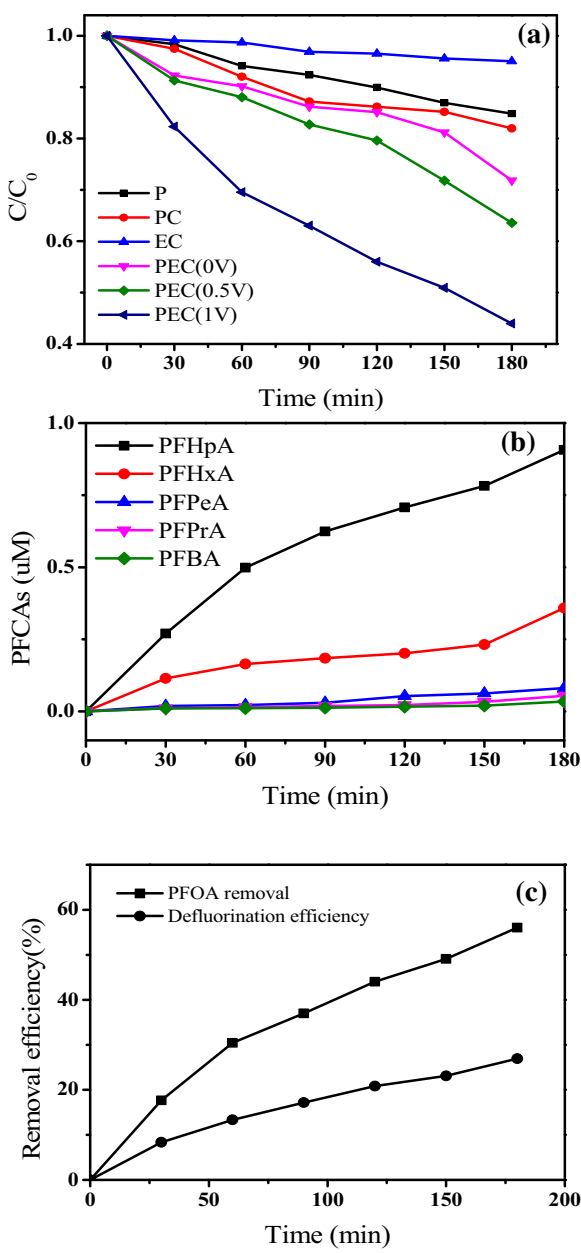


Fig. 7. Proposed PFOA decomposition pathways by C-N-TNTAPEC degradation.

3.4. Degradation of PFOA over C-N-TNTA electrode

Four PFOA removal processes, namely, PEC, PC, EC, and direct photolysis (P), were compared under the illumination of a 100-W Hg lamp at light intensity of 3.12 mW/cm^2 (PEC, PC and P only) and applied voltage of 1.0 V vs. Ag/AgCl (PEC and EC only). As shown in Fig. 7a, the PEC was the most efficient in PFOA degradation among all four methods studied. After 180 min, the PFOA removal was 56.1% at initial concentration of 40 mg/L , whereas only 18.1%, 4.96%, and 15.1% of PFOA removal were achieved by PC, EC, and P processes, respectively. Fig. 7a also shows that the percentage of PFOA degradation was increased with increase in bias potential. It was clearly that the applied bias potential of 1.0 V yielded the highest percentage of PFOA degradation. After 180 min, the percent PFOA degradation was 56.1, 36.4, and 28.1% at applied bias potential of 1.0 , 0.5 , and 0.0 V , respectively. Furthermore, the data could be fitted approximately by a pseudo-first-order kinetic equation: $\ln(C_0/C) = kt$; where C_0 , C , and k are the initial PFOA concentration,

Table 2
Quantified synergistic effect of EC and PC in PEC system.

Applied potential	0 V	0.5 V	1.0 V
Dark current (mA)	0.0012	0.0023	0.033
Photo current (mA)	1.09	2.48	3.10
Total Current (mA)	1.0912	2.4823	3.133
Synergistic (%)	0	56.00	64.16

PFOA concentration at reaction time t , and rate constant, respectively. As shown in Table 2, the reaction rate (e.g., $4.3 \times 10^{-3} \text{ s}^{-1}$) for the system at 1 V of applied bias potential was approximately 3 times that of 0.0 V (e.g., $1.4 \times 10^{-3} \text{ s}^{-1}$) under the same degree of illumination. The difference in PE performance may be attributed to the followings: direct contribution of anodic current to the EC oxidation of PFOA, enhanced separation of photogenerated holes and electrons, and accumulation of holes on the photoanode surface. The rate constant of PFOA degradation was $1.1 \times 10^{-3} \text{ s}^{-1}$ and $4 \times 10^{-4} \text{ s}^{-1}$ via PC and EC, respectively (Table 2). The applied voltage is a key to efficient PFOA degradation in EC. When the applied bias potential was below the redox potential of the target compound; increase in bias potential could increase the PC efficiency by promoting the separation and transfer of photogenerated holes and electrons. Furthermore, when the applied bias potential is greater than the redox potential of the target compound, there will be increase in direct oxidation of the target compounds and the separation of holes and electrons [12]. It can be implied that the photocurrent generated from the C-N-TNTA photoanode is effectively transported to the counter electrode by the external potential, which enhances charge separation. In a two-chamber PEC system, when the applying potential was greater than that of the flat band of C-N-TNTA under illumination the photogenerated current could be transferred through an external circuit to the cathode, which might increase the activity of photogenerated active species, e.g., holes, on the surface of the photoanode by impeding the recombination between photogenerated holes and electrons. Fig. 7b shows the time dependence of short-chain intermediates produced during PEC degradation of PFOA. The amounts of PFHpA, PFHxA, PFPeA, PFPrA, and PFBA (Table S1, Supporting Information) increased with reaction time. Fig. S5 shows the total ion chromatograph (TIC) of perfluorocarbons (PFCs), which suggests a stepwise removal of CF_2 leading to the formation of short-chain PFCs [20].

The defluorination efficiency, η , was determined by $\eta = \left(\frac{C_F^-}{15 \times C_0} \right) \times 100$; where C_F^- and C_0 is final fluoride and the initial PFOA concentration, respectively. Fig. 7c shows that the fluoride concentration increases simultaneously with PFOA decomposition. After 180 min, the extent of defluorination was 26.94% while that of PFOA removal was 56.04%, which indicated that approximately half of the PFOA degraded was transformed to fluoride. Our results are consistent with that reported by Zhao et al. [63], who studied the decomposition of PFOA (initial concentration 40 mg/L) using $\beta\text{-Ga}_2\text{O}_3$ (0.5 g/L) under UV illumination at 254 nm in N_2 atmosphere and reported increase in defluorination efficiency with PFOA decomposition.

Table 3

The corresponding electron lifetime of C-N-TNTAs under different potential (0 V, 0.5 V and 1 V).

Bias potential (V)	Frequency (Hz)	Lifetime (ms)
0.0	63.1	2.52
0.5	39.8	4.01
1.0	25.1	6.34

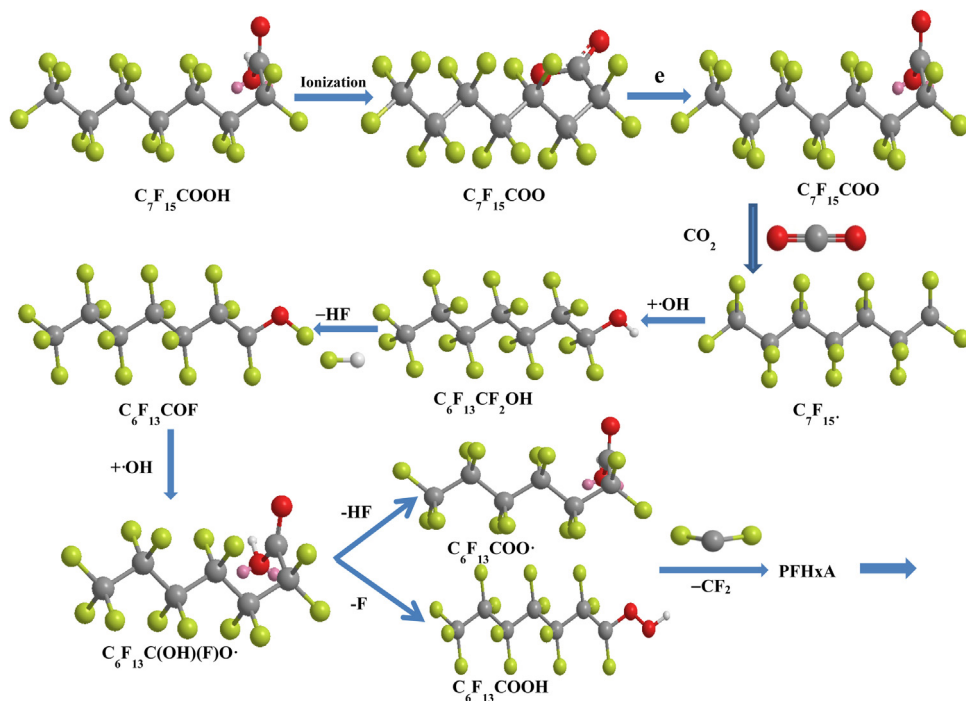
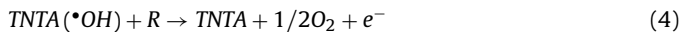
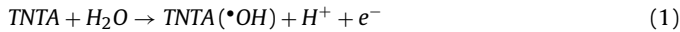


Fig. 8. DMPO spin-trapping electron spin resonance spectra of (a) TNTA and (b) C-N-TNTA for DMPO-•OH and DMPO-CH₃.

3.5. Mechanistic aspects of PFOA degradation over C-N-TNTA electrode in PEC system

Based on results shown in Fig. 6, it is clear that hydroxyl radical is the major species responsible for indirect EC degradation of organic contaminants [12,64]:



where R is PFOA; DP is degradation product(s). The PFOA in the anodic chamber was oxidized (either directly or indirectly by hydroxyl radicals). The PC oxidation ability of C-N-TNTA was enhanced by EC in a PEC system.

The synergistic effect and the contribution of EC and PC to PEC reactions was quantified at 1.1 and 3.1 mA for 0 and 1.0 V bias potential, respectively. In addition, the LC-MS result shows that PFOA was decomposed to short-chain perfluorinated carboxylic acid stepwise. The CF₂ units were flaked and CF₂-less perfluorinated carboxylic acids species were formed (Table 3).

In the present PEC system, electrons were transferred to the cathode to facilitate water reduction to hydrogen and minimized the recombination of photogenerated electrons and holes, thereby enhanced the photon-efficiency, enabled the simultaneous utilization of photogenerated holes and electrons for concurrent oxidation and reduction reactions. Results of Nyquist and Bode plots showed effective separation of the photogenerated electron-hole pairs that accelerated charge transfer and extended the electron lifetime. Ultimately, increasing applied potential facilitated PFOA degradation and H₂O reduction.

Based on the above results (Fig. 6) and literature reported [20,65], a preliminary mechanism for the PEC degradation of PFOA can be proposed (Fig. 8). PFOA, a strong acid ($\text{pK}_a = 2.5$), is present

as an anionic species i.e., C₇F₁₅COO⁻ at neutral pH [66]. The adsorption of C₇F₁₅COO⁻ on the surface of C-N-TNTA photoanode takes place readily. Upon UV irradiation, C₇F₁₅COO⁻ was photocatalytically reduced to C₇F₁₅COO[•], which is photolytically converted to C₇F₁₅[•] and CO₂. Reaction between C₇F₁₅[•] and •OH (generated from photocatalysis of H₂O, i.e., H₂O + h⁺ → OH[•] + H⁺) forms C₇F₁₅OH [67], which underwent HF elimination to form C₆F₁₃COF [20,68]. Further •OH attack of C₆F₁₃COF yields C₆F₁₃C(OH)FO[•]. The cleavage of HF from C₆F₁₃C(OH)FO[•] forms C₆F₁₃COO[•] or C₆F₁₃COOH and F[•]. Subsequent formation of C₆F₁₃COOF (PFHxA) takes places by losing a CF₂ unit to yield C₆F₁₃OH [20]. The C₆F₁₃ and COOH can generate C₆F₁₃[•] by cleaving the C-C bond, which follows reaction routes similar to that of C₇F₁₅ radicals to form PFHxA. The bond cleavage of PFOA was closed to the photo-Kolbe mechanism [67,69,70]. PFOA was decomposed into short-chain perfluorinated carboxylic acid by CF₂ elimination. CF₂-less perfluorinated carboxylic acids species were formed. Numerous researchers have reported the decomposition of PFOA to short-chain PFCA species, such as C₆F₁₃COOH, C₅F₁₁COOH, C₄F₉COOH, C₃F₇COOH, and C₂F₅COOH [25,71]. Our ESR results clearly demonstrate that the active species (•OH and CH₃[•]) are responsible for the PEC decomposition of PFOA, and strongly suggest that the degradation of organic compounds in a PEC system (such as C-N-TNTA photoanode) proceeds through surface intermediates of oxygen reduction or water oxidation. Our findings were also in agreement with Rengifo-Herrera et al. [72] and Fu et al. [59].

3.6. Concurrent hydrogen generation

Fig. S6 shows the hydrogen gas collected as a function of time in the PEC system. The amount of H₂ was 8.30 mmol after 180 min of irradiation time at a biased potential of 1.0 V, which was 2.5 and 2.8 times that of 0.5 and 0 V, respectively. The amount of hydrogen generation in our PEC system was much greater than that reported on the literature of conventional TiO₂ photocatalysis [7]. In a two-chamber PEC system, an increasing bias potential could increase the PC activity by promoting the separation and transfer of photogenerated holes and electrons. Furthermore, C and N codoping promoted electron-hole separation and enabled electrons active

participate in hydrogen generation via the synergistic effect of PC and EC reactions.

4. Conclusion

The synergistic effect of electrochemical and photocatalytic steps on PEC reactions were 0, 56 and 65% at bias potential of 0, 0.5 and 1.0 V, respectively, based on photocurrent measurements. The increase in synergistic efficiency of photoelectrochemical process was the most important promoter for PFOA degradation. ERS results showed the presence of •OH and CH₃• radicals, which were responsible for the degradation of PFOA. Based on LC-MS results, PFOA was decomposed to shorter-chain perfluorinated carboxylic acid stepwise. More CF₂ units could be flaked and CF₂-shortened perfluorinated carboxylic acids species were formed by PEC than PC or EC alone. In the present PEC system, the electrons were transferred to the cathode for water reduction to hydrogen under an applied potential, which minimized the photo-generated electrons and holes recombination that ultimately enhanced the photon-efficiency, enabled simultaneous utilization of photo-generated holes and electrons for concurrent oxidation and reduction reactions.

Acknowledgments

This study was funded by the Pearl River Nova Program of Guangzhou, Guangzhou, China and Fundamental Research Funds for the Central Universities of SCUT, Guangzhou, China and the National Science Council of the Republic of China, Taiwan, for financially supporting this research under Grant No. MOST 103-22218-E-029-001. The authors are also grateful to Mr. Song in SCUT in China for his kind assistance in electrochemical analysis.

Appendix A. Supplementary data

Supplementary data associated with this article can be found, in the online version, at <http://dx.doi.org/10.1016/j.apcatb.2017.02.084>.

References

- [1] Y. Liu, J. Li, B. Zhou, H. Chen, Z. Wang, W. Cai, A TiO₂-nanotube-array-based photocatalytic fuel cell using refractory organic compounds as substrates for electricity generation, *Chem. Commun.* 47 (2011) 10314–10316.
- [2] K.L. Chang, Q. Sun, Y.P. Peng, S.-W. Lai, M. Sung, C.-Y. Huang, H.-W. Kuo, J. Sun, Y.-C. Lin, Cu₂O loaded titanate nanotube arrays for simultaneously photoelectrochemical ibuprofen oxidation and hydrogen generation, *Chemosphere* 150 (2016) 605–614.
- [3] C.A. Grimes, G.K. Mor, *TiO₂ Nanotube Arrays: Synthesis, Properties, and Applications*, Springer, 2009.
- [4] E. Gyorgy, G. Socol, E. Axente, I.N. Mihailescu, C. Ducu, S. Ciucă, Anatase phase TiO₂ thin films obtained by pulsed laser deposition for gas sensing applications, *Appl. Surf. Sci.* 247 (2005) 429–433.
- [5] S. Nakade, T. Kanzaki, S. Kambe, Y.J. Wada, S. Yanagida, Investigation of cation-induced degradation of dye-sensitized solar cells for a new strategy to long-term stability, *Langmuir* 21 (2005) 11414–11417.
- [6] Y. Bai, Y. Cao, J. Zhang, M. Wang, R. Li, P. Wang, S.M. Zakeeruddin, M. Gratzel, High-performance dye-sensitized solar cells based on solvent-free electrolytes produced from eutectic melts, *Nat. Mater.* 7 (2008) 626–630.
- [7] A. Kudo, Y. Miseki, Heterogeneous photocatalyst materials for water splitting, *Chem. Soc. Rev.* 38 (2009) 253–278.
- [8] B. Zhou, M. Schulz, H.Y. Lin, S.I. Shah, J.H. Qu, C.P. Huang, Photoelectrochemical generation of hydrogen over carbon-doped TiO₂ photoanode, *Appl. Catal. B-Environ.* 92 (2009) 41–49.
- [9] R. van de Krol, M. Grätzel, *Photoelectrochemical Hydrogen Production*, Springer, 2011.
- [10] Y.P. Peng, Y.T. Yeh, P.Y. Wang, C. Huang, A solar cell driven electrochemical process for the concurrent reduction of carbon dioxide and degradation of azo dye in dilute KHCO₃ electrolyte, *Sep. Purif. Technol.* 117 (2013) 3–11.
- [11] X. Lu, G. Wang, T. Zhai, M. Yu, J. Gan, Y. Tong, Y. Li, Hydrogenated TiO₂ nanotube arrays for supercapacitors, *Nano Lett.* 12 (2012) 1690–1696.
- [12] X. Zhao, Y.F. Zhu, Synergetic degradation of rhodamine B at a porous ZnWO₄ film electrode by combined electro-oxidation and photocatalysis, *Environ. Sci. Technol.* 40 (2006) 3367–3372.
- [13] R.T. Pelegri, R.S. Freire, N. Duran, R. Bertazzoli, Photoassisted electrochemical degradation of organic pollutants on a DSA type oxide electrode: process test for a phenol synthetic solution and its application for the E1 bleach kraft mill effluent, *Environ. Sci. Technol.* 35 (2001) 2849–2853.
- [14] X. Zhao, J.H. Qu, H.J. Liu, C. Hu, Photoelectrocatalytic degradation of triazine-containing azo dyes at gamma-Bi2MoO6 film electrode under visible light irradiation lambda > 420 nm, *Environ. Sci. Technol.* 41 (2007) 6802–6807.
- [15] J.P. Giesy, K. Kannan, Global distribution of perfluorooctane sulfonate in wildlife, *Environ. Sci. Technol.* 35 (2001) 1339–1342.
- [16] K. Kannan, S. Corsolini, J. Falandysz, G. Fillmann, K.S. Kumar, B.G. Loganathan, M.A. Mohd, J. Olivero, N.V. Wouwe, J.H. Yang, Perfluorooctanesulfonate and related fluorocompounds in human blood from several countries, *Environ. Sci. Technol.* 38 (2004) 4489–4495.
- [17] A.A. Jensen, H. Leffers, Emerging endocrine disruptors: perfluoroalkylated substances, *Int. J. Androl.* 31 (2008) 161–169.
- [18] G.L. Kennedy, J.B. Butenhoff, G.W. Olsen, J.C. O'Connor, A.M. Seacat, R.G. Perkins, L.B. Biegel, S.R. Murphy, D.G. Farrar, The toxicology of perfluorooctanoate, *Crit. Rev. Toxicol.* 34 (2004) 351–384.
- [19] B.D. Key, R.D. Howell, C.S. Criddle, Fluorinated organics in the biosphere, *Environ. Sci. Technol.* 31 (1997) 2445–2454.
- [20] H. Hori, E. Hayakawa, H. Einaga, S. Kutsuna, K. Koike, T. Ibusuki, H. Kiatagawa, R. Arakawa, Decomposition of environmentally persistent perfluorooctanoic acid in water by photochemical approaches, *Environ. Sci. Technol.* 38 (2004) 6118–6124.
- [21] C.C. Tsai, H. Teng, Structural features of nanotubes synthesized from NaOH treatment on TiO₂ with different post-treatments, *Chem. Mater.* 18 (2006) 367–373.
- [22] Y.T. Tsai, A.Y.C. Lin, Y.H. Weng, K.C. Li, Treatment of perfluorinated chemicals by electro-microfiltration, *Environ. Sci. Technol.* 44 (2010) 7914–7920.
- [23] S. Takagi, F. Adachi, K. Miyano, Y. Koizumi, H. Tanaka, I. Watanabe, S. Tanabe, K. Kannan, Fate of perfluorooctanesulfonate and perfluorooctanoate in drinking water treatment processes, *Water Res.* 45 (2011) 3925–3932.
- [24] X. Li, S. Chen, X. Quan, Y. Zhang, Enhanced adsorption of PFOA and PFOS on multiwalled carbon nanotubes under electrochemical assistance, *Environ. Sci. Technol.* 45 (2011) 8498–8505.
- [25] H. Hori, A. Yamamoto, E. Hayakawa, S. Taniyasu, N. Yamashita, S. Kutsuna, H. Kiatagawa, R. Arakawa, Efficient decomposition of environmentally persistent perfluorocarboxylic acids by use of persulfate as a photochemical oxidant, *Environ. Sci. Technol.* 39 (2005) 2383–2388.
- [26] H. Hori, Y. Nagaoka, A. Yamamoto, T. Sano, N. Yamashita, S. Taniyasu, S. Kutsuna, I. Osaka, R. Arakawa, Efficient decomposition of environmentally persistent perfluorooctanesulfonate and related fluorochemicals using zerovalent iron in subcritical water, *Environ. Sci. Technol.* 40 (2006) 1049–1054.
- [27] Q. Zhuo, S. Deng, B. Yang, J. Huang, G. Yu, Efficient electrochemical oxidation of perfluorooctanoate using a Ti/SnO₂-Sb-Bi anode, *Environ. Sci. Technol.* 45 (2011) 2973–2979.
- [28] H. Lin, J. Niu, J. Xu, H. Huang, D. Li, Z. Yue, C. Feng, Highly efficient and mild electrochemical mineralization of long-chain perfluorocarboxylic acids (C₉–C₁₀) by Ti/SnO₂-Sb-Ce, Ti/SnO₂-Sb/Ce-PbO₂, and Ti/BDD Electrodes, *Environ. Sci. Technol.* 47 (2013) 13039–13046.
- [29] J. Niu, H. Lin, J. Xu, H. Wu, Y. Li, Electrochemical mineralization of perfluorocarboxylic acids (PFCAs) by Ce-doped modified porous nanocrystalline PbO₂ film electrode, *Environ. Sci. Technol.* 46 (2012) 10191–10198.
- [30] B. Yang, C. Jiang, G. Yu, Q. Zhuo, S. Deng, J. Wu, H. Zhang, Highly efficient electrochemical degradation of perfluorooctanoic acid (PFOA) by F-doped Ti/SnO₂ electrode, *J. Hazard. Mater.* 299 (2015) 417–424.
- [31] M. Bellardita, M. Addamo, A. Di Paola, L. Palmisano, A.M. Venezia, Preparation of N-doped TiO₂: characterization and photocatalytic performance under UV and visible light, *Phys. Chem. Chem. Phys.* 11 (2009) 4084–4093.
- [32] G.S. Shao, F.Y. Wang, T.Z. Ren, Y.P. Liu, Z.Y. Yuan, Hierarchical mesoporous phosphorus and nitrogen doped titania materials: synthesis, characterization and visible-light photocatalytic activity, *Appl. Catal. B-Environ.* 92 (2009) 61–67.
- [33] Y.P. Peng, S.L. Lo, F.H. Ou, S.W. Lai, Microwave-assisted hydrothermal synthesis of N-doped titanate nanotubes for visible-light-responsive photocatalysis, *J. Hazard. Mater.* 183 (2010) 754–758.
- [34] H.H. Ou, S.L. Lo, C.H. Liao, N-doped TiO₂ prepared from microwave-assisted titanate nanotubes (NaxH₂-xTi₃O₇): the effect of microwave irradiation during TNT synthesis on the visible light photoactivity of n-doped TiO₂, *J. Phys. Chem. C* 115 (2011) 4000–4007.
- [35] S. Livraghi, M.R. Chierotti, E. Giannello, G. Magnacca, M.C. Paganini, G. Cappelletti, C.L. Bianchi, Nitrogen-doped titanium dioxide active in photocatalytic reactions with visible light: a multi-technique characterization of differently prepared materials, *J. Phys. Chem. C* 112 (2008) 17244–17252.
- [36] R. Asahi, T. Morikawa, T. Ohwaki, K. Aoki, Y. Taga, Visible-light photocatalysis in nitrogen-doped titanium oxides, *Science* 293 (2001) 269–271.
- [37] C. Chen, H. Bai, C. Chang, Effect of plasma processing gas composition on the nitrogen-doping status and visible light photocatalysis of TiO₂, *J. Phys. Chem. C* 111 (2007) 15228–15235.

- [38] X. Wang, J.C. Yu, Y. Chen, L. Wu, X. Fu, ZrO₂-Modified mesoporous nanocrystalline TiO_{2-x}N x as efficient visible light photocatalysts, *Environ. Sci. Technol.* 40 (2006) 2369–2374.
- [39] G. Dai, S. Liu, H. Liu, A simple preparation of carbon and nitrogen co-doped nanoscaled TiO₂ with exposed {001} facets for enhanced visible-light photocatalytic activity, *J. Mol. Catal. A: Chem.* 368–369 (2012) 38–42.
- [40] V. Luca, S. Djajanti, R.F. Howe, Structural and electronic properties of sol-gel titanium oxides studied by X-ray absorption spectroscopy, *J. Phys. Chem. B* 102 (1998) 10650–10657.
- [41] T. Rajh, J.M. Nedeljkovic, L.X. Chen, O. Poluektov, M.C. Thurnauer, Improving optical and charge separation properties of nanocrystalline TiO₂ by surface modification with vitamin C, *J. Phys. Chem. B* 103 (1999) 3515–3519.
- [42] Z. Wu, G. Ouvrard, P. Gressier, C. Natoli, Ti and OK edges for titanium oxides by multiple scattering calculations: comparison to XAS and EELS spectra, *Phys. Rev. B* 55 (1997) 10382.
- [43] A. Nakahira, T. Kubo, C. Numako, Formation mechanism of TiO₂-derived titanate nanotubes prepared by the hydrothermal process, *Inorg. Chem.* 49 (2010) 5845–5852.
- [44] D. Wang, L. Liu, X. Sun, T.K. Sham, Observation of lithiation-induced structural variations in TiO₂ nanotube arrays by X-ray absorption fine structure, *J. Mater. Chem. A* 3 (2015) 412–419.
- [45] H. Yamashita, S. Kawasaki, Y. Ichihashi, M. Harada, M. Takeuchi, M. Anpo, G. Stewart, M.A. Fox, C. Louis, M. Che, Characterization of titanium-silicon binary oxide catalysts prepared by the sol-gel method and their photocatalytic reactivity for the liquid-phase oxidation of 1-octanol, *J. Phys. Chem. B* 102 (1998) 5870–5875.
- [46] M. Che, K. Mori, H. Yamashita, Elaboration, characterization and properties of silica-based single-site heterogeneous photocatalysts, *Proc. R. Soc. A* (2012), pp. rspa 20120139.
- [47] Y. Kuwahara, T. Ohmichi, K. Mori, I. Katayama, H. Yamashita, Synthesis of zeolite from steel slag and its application as a support of nano-sized TiO₂ photocatalyst, *J. Mater. Sci.* 43 (2007) 2407–2410.
- [48] T.A. Saleh, V.K. Gupta, Photo-catalyzed degradation of hazardous dye methyl orange by use of a composite catalyst consisting of multi-walled carbon nanotubes and titanium dioxide, *J. Colloid Interface Sci.* 371 (2012) 101–106.
- [49] M. Ye, J. Gong, Y. Lai, C. Lin, Z. Lin, High-efficiency photoelectrocatalytic hydrogen generation enabled by palladium quantum dots-sensitized TiO₂ nanotube arrays, *J. Am. Chem. Soc.* 134 (2012) 15720–15723.
- [50] X. Cheng, W. Leng, D. Liu, Y. Xu, J. Zhang, C. Cao, Electrochemical preparation and characterization of surface-fluorinated TiO₂ nanoporous film and its enhanced photoelectrochemical and photocatalytic properties, *J. Phys. Chem. C* 112 (2008) 8725–8734.
- [51] Q. Kang, J. Cao, Y. Zhang, L. Liu, H. Xu, J. Ye, Reduced TiO₂ nanotube arrays for photoelectrochemical water splitting, *J. Mater. Chem. A* 1 (2013) 5766–5774.
- [52] D. Hwang, H. Lee, S.-Y. Jang, S.M. Jo, D. Kim, Y. Seo, D.Y. Kim, Electrospray preparation of hierarchically-structured mesoporous TiO₂ spheres for use in highly efficient dye-sensitized solar cells, *ACS Appl. Mater. Interfaces* 3 (2011) 2719–2725.
- [53] M. Ye, D. Zheng, M. Lv, C. Chen, C. Lin, Z. Lin, Hierarchically structured nanotubes for highly efficient dye-sensitized solar cells, *Adv. Mater.* 25 (2013) 3039–3044.
- [54] R. Beranek, H. Tsuchiya, T. Sugishima, J. Macak, L. Taveira, S. Fujimoto, H. Kisch, P. Schmuki, Enhancement and limits of the photoelectrochemical response from anodic TiO₂ nanotubes, *Appl. Phys. Lett.* 87 (2005) 243114.
- [55] Q. Kang, J. Cao, Y. Zhang, L. Liu, H. Xu, J. Ye, Reduced TiO₂ nanotube arrays for photoelectrochemical water splitting, *J. Mater. Chem. A* 1 (2013) 5766–5774.
- [56] H. Tsuchiya, J.M. Macak, A. Ghicov, A.S. Räder, L. Taveira, P. Schmuki, Characterization of electronic properties of TiO₂ nanotube films, *Corros. Sci.* 49 (2007) 203–210.
- [57] A. Hagfeldt, M. Graetzel, Light-induced redox reactions in nanocrystalline systems, *Chem. Rev. (United States)* 95 (1995).
- [58] G. Liu, J. Zhao, H. Hidaka, ESR spin-trapping detection of radical intermediates in the TiO₂-assisted photo-oxidation of sulforhodamine B under visible irradiation, *J. Photochem. Photobiol. A: Chem.* 133 (2000) 83–88.
- [59] H. Fu, L. Zhang, S. Zhang, Y. Zhu, J. Zhao, Electron spin resonance spin-trapping detection of radical intermediates in N-doped TiO₂-assisted photodegradation of 4-chlorophenol, *J. Phys. Chem. B* 110 (2006) 3061–3065.
- [60] J. Pan, X. Li, Q. Zhao, T. Li, M. Tade, S. Liu, Construction of Mn_{0.5}Zn_{0.5}Fe₂O₄ modified TiO₂ nanotube array nanocomposite electrodes and their photoelectrocatalytic performance in the degradation of 2,4-DCP, *J. Mater. Chem. C* (2015).
- [61] M.R. Hoffmann, S.T. Martin, W. Choi, D.W. Bahnemann, Environmental applications of semiconductor photocatalysis, *Chem. Rev.* 95 (1995) 69–96.
- [62] E. Bae, W. Choi, J. Park, H.S. Shin, S.B. Kim, J.S. Lee, Effects of surface anchoring groups (carboxylate vs phosphonate) in ruthenium-complex-sensitized TiO₂ on visible light reactivity in aqueous suspensions, *J. Phys. Chem. B* 108 (2004) 14093–14101.
- [63] B. Zhao, P. Zhang, Photocatalytic decomposition of perfluoroctanoic acid with β-Ga₂O₃ wide bandgap photocatalyst, *Catal. Commun.* 10 (2009) 1184–1187.
- [64] M. Zhou, Q. Dai, L. Lei, C.a. Ma, D. Wang, Long life modified lead dioxide anode for organic wastewater treatment: electrochemical characteristics and degradation mechanism, *Environ. Sci. Technol.* 39 (2004) 363–370.
- [65] Y.C. Chen, S.L. Lo, J. Kuo, Effects of titanate nanotubes synthesized by a microwave hydrothermal method on photocatalytic decomposition of perfluoroctanoic acid, *Water Res.* 45 (2011) 4131–4140.
- [66] D.C. Burns, D.A. Ellis, H. Li, C.J. McMurdo, E. Webster, Experimental pKa determination for perfluoroctanoic acid (PFOA) and the potential impact of pKa concentration dependence on laboratory-measured partitioning phenomena and environmental modeling, *Environ. Sci. Technol.* 42 (2008) 9283–9288.
- [67] J. Chen, P.Y. Zhang, J. Liu, Photodegradation of perfluoroctanoic acid by 185 nm vacuum ultraviolet light, *J. Environ. Sci.* 19 (2007) 387–390.
- [68] J. Chen, P. Zhang, Photodegradation of perfluoroctanoic acid in water under irradiation of 254 nm and 185 nm light by use of persulfate, *Water Sci. Technol.* 54 (2006) 317–325.
- [69] L. Ravichandran, K. Selvam, M. Muruganandham, M. Swaminathan, Photocatalytic cleavage of C-F bond in pentafluorobenzoic acid with titanium dioxide-P25, *J. Fluorine Chem.* 127 (2006) 1204–1210.
- [70] R. Dillert, D. Bahnemann, H. Hidaka, Light-induced degradation of perfluorocarboxylic acids in the presence of titanium dioxide, *Chemosphere* 67 (2007) 785–792.
- [71] H. Moriwaki, Y. Takagi, M. Tanaka, K. Tsuruho, K. Okitsu, Y. Maeda, Sonochemical decomposition of perfluoroctane sulfonate and perfluoroctanoic acid, *Environ. Sci. Technol.* 39 (2005) 3388–3392.
- [72] J.A. Rengifo-Herrera, K. Pierzchała, A. Sienkiewicz, L. Forró, J. Kiwi, C. Pulgarin, Abatement of organics and Escherichia coli by N, S co-doped TiO₂ under UV and visible light. Implications of the formation of singlet oxygen (¹O₂) under visible light, *Appl. Catal. B: Environ.* 88 (2009) 398–406.